

Electronic structure reconstruction by orbital symmetry breaking in IrTe₂

D. Ootsuki¹, S. Pyon², K. Kudo², M. Nohara², M. Horio³, T. Yoshida³, A. Fujimori³,
M. Arita⁴, H. Anzai⁴, H. Namatame⁴, M. Taniguchi^{4,5}, N. L. Saini^{6,1}, and T. Mizokawa¹

¹*Department of Complexity Science and Engineering & Department of Physics,
University of Tokyo, 5-1-5 Kashiwanoha, Chiba 277-8561, Japan*

²*Department of Physics, Okayama University, Kita-ku, Okayama 700-8530, Japan*

³*Department of Physics, University of Tokyo, 7-3-1 Hongo, Tokyo 113-0033, Japan*

⁴*Hiroshima Synchrotron Radiation Center, Hiroshima University, Higashi-hiroshima 739-0046, Japan*

⁵*Graduate School of Science, Hiroshima University, Higashi-hiroshima 739-8526, Japan and*

⁶*Department of Physics, University of Roma "La Sapienza" Piazzale Aldo Moro 2, 00185 Roma, Italy*

(Dated: July 12, 2012)

We report an angle-resolved photoemission spectroscopy (ARPES) study on IrTe₂ which exhibits an interesting lattice distortion below 270 K and becomes triangular lattice superconductors by suppressing the distortion via chemical substitution or intercalation. ARPES results at 300 K show multi-band Fermi surfaces with six-fold symmetry which are basically consistent with band structure calculations. At 20 K in the distorted phase, whereas the flower shape of the outermost Fermi surface does not change from that at 300 K, topology of the inner Fermi surfaces is strongly modified by the lattice distortion. The Fermi surface reconstruction by the distortion depends on the orbital character of the Fermi surfaces, suggesting importance of Ir 5*d* and/or Te 5*p* orbital symmetry breaking.

PACS numbers: 74.70.Xa, 74.25.Jb, 71.30.+h, 71.20.-b

Transition-metal compounds with multi-band Fermi surfaces often exhibit rich and interesting physical properties such as spin-charge-orbital order and superconductivity which originate from topology of their multi-band Fermi surfaces. For example, the multi-orbital electronic structures of transition-metal oxides and chalcogenides including CuIr₂S₄ and Ca_{2-x}Sr_xRuO₄ provide various metal-insulator transitions with spin-charge-orbital orders [1–4]. Also the multi-band structure of the Fe 3*d* orbitals play important roles in superconductivity and magnetism of Fe pnictides and chalcogenides such as LaFeAsO_{1-x}F_x [5]. Recently, Pyon *et al.* [6] and Yang *et al.* [7] have discovered interesting interplay between lattice distortion and superconductivity in triangular lattice IrTe₂ in which multi-band Fermi surfaces are expected to play significant roles. IrTe₂ exhibits a structural phase transition at ~ 270 K from the trigonal (P3m-1) to the monoclinic (C2/m) structure accompanied by anomalies of electrical resistivity and magnetic susceptibility [8]. When the lattice distortion is suppressed by chemical substitution of Pt or Pd for Ir or intercalation of Pd, IrTe₂ becomes superconductors [6, 7].

An electron diffraction result by Yang *et al.* shows that the structural transition is accompanied by superstructure with wave vector of $q = (1/5, 0, -1/5)$. Such superstructure can be explained by charge density wave (CDW) driven by perfect or partial nesting of multi-band Fermi surfaces [7]. In multi-band Fermi surfaces with Ir 5*d* and Te 5*p* orbital degeneracy, the nesting character can be enhanced by orbitally-induced Peierls mechanism [9]. In addition, charge modulation of Ir 5*d* electrons is indicated by an Ir 4*f* x-ray photoemission study [10]. On the other hand, a recent optical study by Fang *et al.* on

single crystal samples shows that there is no gap opening expected for CDW and, instead, band structure is reconstructed over a broad energy scale up to ~ 2 eV [11]. Fang *et al.* conclude that the structural transition of IrTe₂ is not of CDW type but of a novel type driven by Te 5*p* holes [11].

In this context, it is very interesting and important to study geometry of multi-band Fermi surfaces of IrTe₂ using angle-resolved photoemission spectroscopy (ARPES). The present ARPES study shows that, above the transition temperature, the observed Fermi surfaces and band dispersions are consistent with the band structure calculations. The flower-shaped outer Fermi surface and the inner Fermi surfaces like six connected beads are identified. Across the structural transition, whereas the flower shape of the outer Fermi surface does not change appreciably, the topology of the inner Fermi surfaces is strongly modified. Below the transition temperature, the inner Fermi surfaces consist of two straight portions, suggesting Fermi surface nesting. However, gap opening expected for CDW is not observed in the ARPES spectra, consistent with the optical study [11]. Instead, spectral weight is partially suppressed at specific points of the straight Fermi surfaces.

The single crystal samples of IrTe₂ were prepared using a self-flux method [11, 12]. The photoemission measurements were performed at beamline 9A, Hiroshima Synchrotron Radiation Center using a SCIENTA R4000 analyzer with circularly polarized light. The total energy resolution was set to 18 meV for excitation energy of $h\nu = 23$ eV. The angular resolution was set to $\sim 0.3^\circ$ that gives the momentum resolution of $\sim 0.015 \text{ \AA}^{-1}$ for $h\nu = 23$ eV. The incident beam is 50° off the sample surface. The base

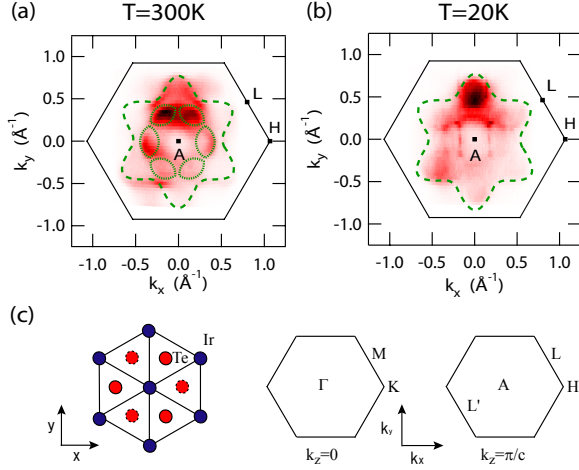


FIG. 1: (color online) Fermi surface mapping of IrTe₂ for $h\nu = 23$ eV taken (a) at 300 K and (b) at 20 K. The hexagonal Brillouin zone boundary is shown by solid lines. The center of the hexagon roughly corresponds to the A point for $h\nu = 23$ eV. For 300 K, the flower-shaped outer Fermi surface and the inner Fermi surfaces with six-fold symmetry are schematically shown by the dashed and dotted curves, respectively. (c) Schematic drawings for the Ir triangular lattice and the hexagonal Brillouin zone at $k_z = 0$ and π/c .

pressure of the spectrometer was in the 10^{-9} Pa range. The samples were cleaved at 300 K under the ultrahigh vacuum and cooled across the structural transition, and then warmed to 300 K to check the reproducibility at 300 K. The samples were oriented by *ex situ* Laue measurements. The spectra were acquired within 8 hours after the cleavage. The binding energy was calibrated using the Fermi edge of gold reference samples.

Figure 1(a) shows the Fermi surface mapping of IrTe₂ at 300 K above the structural transition temperature. The ARPES data are taken at $h\nu = 23$ eV and, for the Fermi surface mapping, the ARPES intensity is integrated within an energy window of ± 5 meV at the Fermi level (E_F). At $h\nu = 23$ eV, the momentum perpendicular to the Ir plane approximately corresponds to π/c , where

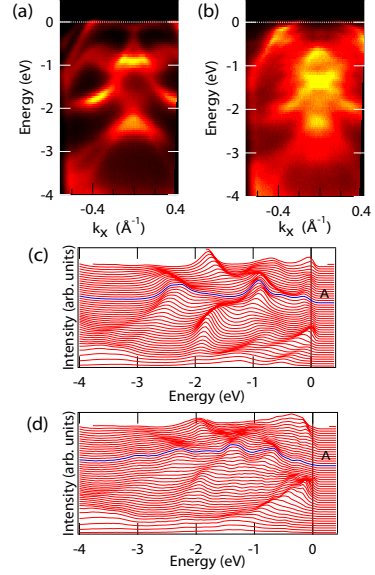


FIG. 2: (color online) Broad-range band dispersions along the A-H direction of IrTe₂ for $h\nu = 23$ eV taken (a) at 300 K and (b) at 20 K. Broad-range energy distribution curves along the A-H direction of IrTe₂ for $h\nu = 23$ eV taken (c) at 300 K and (d) at 20 K.

c is the out-of-plane lattice constant. Therefore, the center of the hexagonal Brillouin zone is the A point. The direction from the A point to the L (H) point corresponds to the direction of Ir-Ir (Ir-Te) bond. In agreement with the band structure calculations [7, 11], the flower-shaped outer Fermi surface with six-fold symmetry is observed as shown by the dashed curve in Fig. 1(a). In addition, the inner Fermi surfaces like six connected beads can be identified as indicated by the dotted curves although effect of thermal excitations at 300 K tends to obscure the relatively small Fermi pockets. The inner Fermi surfaces observed around the A point at 300 K are roughly consistent with the prediction of band-structure calculations [7, 11].

The Fermi surface mapping at 20 K well below the transition temperature is displayed in Fig. 1(b). Across the structural transition, the flower shape of the outer Fermi surface does not change appreciably. However, in the region where the outer Fermi surface is close to the inner Fermi surfaces, while the outer Fermi surface is separated from the inner Fermi surfaces at 300 K, the outer Fermi surface overlaps with the inner Fermi surfaces at 20 K. In contrast to the small effect on the outer Fermi sur-

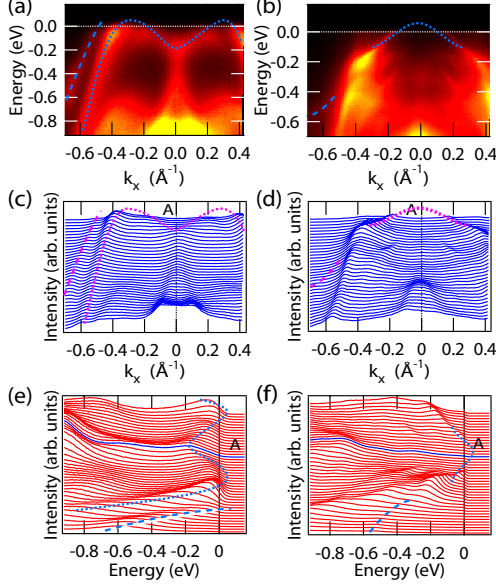


FIG. 3: (color online) Near- E_F band dispersions along the A-H direction of IrTe₂ for $h\nu = 23$ eV taken (a) at 300 K and (b) at 20 K. Near- E_F momentum distribution curves along the A-H direction of IrTe₂ for $h\nu = 23$ eV taken (c) at 300 K and (d) at 20 K. Near- E_F energy distribution curves along the A-H direction of IrTe₂ for $h\nu = 23$ eV taken (e) at 300 K and (f) at 20 K. The outer hole bands and the inner hole-like bands are indicated by the dashed and dotted curves, respectively.

face, the inner Fermi surfaces dramatically change their shapes by the structural transition. It is expected that the outer Fermi surface is mainly constructed from the Ir 5d a_{1g} [$\frac{1}{\sqrt{3}}(XY + YZ + ZX)$] and Te 5p_z orbitals, and that the inner Fermi surfaces mainly have the Ir 5d e'_g [$\frac{1}{\sqrt{3}}(XY + e^{\pm 2\pi i/3}YZ + e^{\pm 4\pi i/3}ZX)$] and Te 5p_{x,y} orbital components (Here, the X-, Y-, and Z-axes are along the three Ir-Te bonds of a regular IrTe₆ octahedron). The ARPES result that the inner Fermi surfaces are more strongly affected by the structural transition is consistent with the band structure calculation by Fang *et al* [11]. However, the geometry of inner Fermi surfaces at 20 K deviates from the prediction of the calculation. Interestingly, two straight portions of Fermi surfaces are

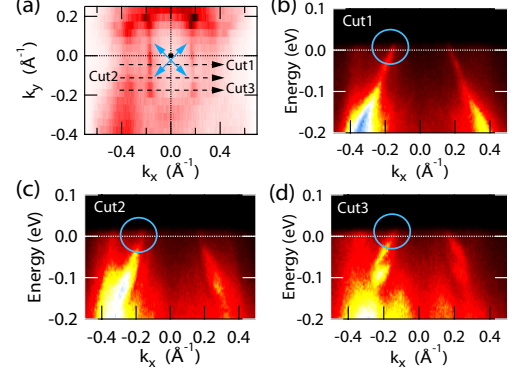


FIG. 4: (color online) (a) Fermi surface mapping near the A point at 20 K for $h\nu = 23$ eV. (b-d) Near- E_F band dispersions along the cuts parallel to the A-H direction at 20 K for $h\nu = 23$ eV.

observed at 20 K. The straight portions are perpendicular to the A-H direction or the direction of Ir-Te bond. Therefore, both of the Te 5p and Ir 5d orbitals would be involved in the structural transition if the straight Fermi surfaces are driven by orbitally-induced Peierls mechanism [9].

Figures 2(a) and (b) show the broad-range band dispersions along the A-H direction at 300 K and 20 K, respectively. Whereas the broad-range band dispersions at 300 K roughly agree with the predictions of the band-structure calculations, those at 20 K deviate from the predictions [7, 11]. In going from 300 K to 20 K, broad-range band structures up to -3 eV are largely modified, which is consistent with the optical study [11]. The broad-range spectral change is more clearly seen in the energy distribution curves for 300 K and 20 K shown in Figs. 2(c) and (d), respectively. In going from 300 K to 20 K, spectral peaks at 300 K tend to be split into several structures at 20 K probably due to complicated

charge and orbital orders. Consequently, in the energy range from -0.2 eV to -3 eV, the spectral peaks at 20 K are much broader than those at 300 K.

On the other hand, spectral peaks from E_F to -0.2 eV are rather sharp at 20 K compared to those at 300 K as shown in Fig. 3. For 300 K, the outer hole band is indicated by the dashed curve in Fig. 3(a) which form the flower-shaped outer Fermi surface of Fig. 1(a). The inner hole-like band indicated by the dotted curves in Fig. 3(a) creates the hole pockets which corresponds to the inner Fermi surfaces of Fig. 1(a). The comparison between Figs. 3(a) and (b) shows that the inner hole-like band is strongly affected by the structural transition. The band located around ~ -0.15 eV of the A point at 300 K disappears at 20 K probably because it is shifted above E_F . Consequently, the hole band indicated by the dotted curve in Fig. 3(b) crosses E_F at 20 K and form the straight portions of the Fermi surfaces of Fig. 1(b). In addition, at 20 K, the outer hole band overlaps with the inner hole bands along the A-H direction. The kink structure of the inner hole band at ~ -0.2 eV is probably due to spin-orbit mixing between the outer hole band and the inner hole band.

The Fermi surface mapping around the A point at 20 K is shown in Fig. 4(a). Interestingly, spectral weight at E_F is partially suppressed at specific points of the straight Fermi surfaces. In cuts 1 and 3 along the A-H direction [Figs. 4(b) and (d)], the hole band clearly crosses E_F and the spectral weight at E_F is not suppressed. On the other hand, in cut 2 [Fig. 4(c)], the intensity of hole band is suppressed near E_F . There are four points where the spectral weight at E_F is suppressed as seen in Fig. 4(a). Such spectral weight suppression at the specific points (cold spots) would be related to the origin of the superstructure. The wave vectors connecting the two cold spots [indicated by the arrows in Fig. 4(a)] are approximately 2/5 of the A-L distance or 1/5 of the L-L' distance, partly consistent with the period of the superstructure.

In conclusion, above the transition temperature, the observed Fermi surfaces and band dispersions are consistent with the band structure calculations. The flower-shaped outer Fermi surface (hole character) with six-fold symmetry and the inner Fermi surfaces (hole pockets) are identified. Across the structural transition, whereas the flower shape of the outer Fermi surface does not change appreciably, the geometry of the inner Fermi surfaces

is strongly modified. In the distorted phase, the inner Fermi surfaces consist of two straight portions, suggesting that nesting character is enhanced. However, the gap opening expected for CDW is not observed in the ARPES spectra, consistent with the optical study. Also the electronic structure up to ~ -3 eV is reconstructed by the lattice distortion, which is also consistent with the optical study. In addition, the spectral weight at E_F is suppressed at the specific points of the straight Fermi surfaces, which would be related to the origin of the superstructure.

The authors would like to thank valuable discussions with D. I. Khomskii and H. Takagi. This work was partially supported by a Grants-in-Aid for Young Scientists (B) (23740274, 24740238) from the Japan Society of the Promotion of Science (JSPS) and the Funding Program for World-Leading Innovative R&D on Science and Technology (FIRST Program) from JSPS. The synchrotron radiation experiment was performed with the approval of HSRC (Proposal No.12-A-12).

-
- [1] M. Imada, A. Fujimori, Y. Tokura, *Rev. Mod. Phys.* **70**, 1039 (1998).
 - [2] S. Nagata, T. Hagino, Y. Seki, and T. Bitoh, *Physica B* **194 – 196**, 1077 (1994).
 - [3] P. G. Radaelli, Y. Horibe, M. J. Gutmann, H. Ishibashi, C. H. Chen, R. M. Ibberson, Y. Koyama, Y. S. Hor, V. Kirykhin, and S. W. Cheong, *Nature* **416**, 155 (2002).
 - [4] S. Nakatsuji and Y. Maeno, *Phys. Rev. Lett.* **84**, 2666 (2000).
 - [5] Y. Kamihara, T. Watanabe, M. Hirano, and H. Hosono, *J. Am. Chem. Soc.* **130**, 3296 (2008).
 - [6] S. Pyon, K. Kudo, and M. Nohara, *J. Phys. Soc. Jpn.* **81**, 053701 (2012).
 - [7] J. J. Yang, Y. J. Choi, Y. S. Oh, A. Hogan, Y. Horibe, K. Kim, B. I. Min, and S-W. Cheong, *Phys. Rev. Lett.* **108**, 116402 (2012).
 - [8] N. Matsumoto, K. Taniguchi, R. Endoh, H. Takano, and S. Nagata, *J. Low Temp. Phys.* **117**, 1129 (1999).
 - [9] D. I. Khomskii and T. Mizokawa, *Phys. Rev. Lett.* **94**, 156402 (2005).
 - [10] D. Ootsuki, Y. Wakisaka, S. Pyon, K. Kudo, M. Nohara, and T. Mizokawa, to be published in *Phys. Rev. B*.
 - [11] A. F. Fang, G. Xu, T. Dong, P. Zheng, and N. L. Wang, arXiv:1203.4061.
 - [12] S. Pyon, K. Kudo, and M. Nohara, unpublished.